FULL RESEARCH ARTICLE

Recoater crashes during powder bed fusion of metal with laser beam: simulative prediction of interference and experimental evaluation of resulting part quality

Stefan Brenner[1,3] · Martin Moser[1,3] · Lea Strauß[2,3] · Vesna Nedeljkovic-Groha[1,3] · Günther Löwisch[2,3]

Abstract

In powder bed fusion of metal with laser beam (PBF-LB/M), repetitive melting and solidification of newly added layers lead to thermal stresses and distortions during part build-up. Particularly at critical component features such as unsupported overhangs, super-elevated edges pose a risk in terms of crashes with the recoating system during powder spreading. Damaged recoater lips lead to irregularities in the form of stripes in the powder bed. These local inhomogeneities cause lack-of-fusion porosity and geometric defects on the part surface. However, quantitative information on important quality aspects, such as tensile properties, dimensional accuracy, roughness, and hardness of parts printed under irregular powder bed conditions is scarce. Here, we show that samples from build jobs with recoater crashes maintain their elastic tensile properties and hardness, but lose elongation at break. Finite-element simulations of in-process distortions are used to design an artifact that intentionally damages the silicone rubber lip of the recoater but does not cause machine breakdown. The lowest mean yield strength of the damage-affected samples is 243 MPa, which is still within the material data sheet limits for AlSi10Mg. Therefore, recoater crashes do not necessarily result in rejects, but users must consider the likely presence of porosity.

Keywords Powder bed fusion of metal with laser beam · AlSi10Mg · Recoater crash · Powder bed irregularity · Part quality

1 Introduction

Powder bed fusion of metal with laser beam (PBF-LB/M) has found acceptance for industrial production of critical parts in aerospace, medical, energy, and automotive applications [1]. Drawbacks of the locally focused laser energy input are the initiation of the temperature gradient mechanism and the associated plastification that cause residual stresses and part distortions [2]. Unacceptable large distortions can result in build failure or rejection [3].

Part edges warped above the powder bed level, referred to as super-elevation [4, 5], pose a risk to the stability of the process in the form of collisions between the recoating mechanism and the part [6, 7]. Morante et al. [8] sum up recoater crashes as possible causes of problems like incomplete parts, geometric and surface defects, porosity, and microstructural inhomogeneity. Powder bed irregularities, such as super-elevated part edges or powder trenches, can also lead to reduced part properties and therefore rejection of the parts [9, 10].

To account for these process-related phenomena, the finite-element (FE) method offers sophisticated approaches. The simulation of component scale residual stresses, distortions, and recoater collisions are currently the most mature domains of modeling [11]. Many commercially available FE simulation tools offer the possibility to predict recoater crashes [12].

Since process errors still occur, process monitoring is often used to detect and classify powder bed irregularities. Comprehensive review articles on in-situ monitoring methods and the detection of powder bed irregularities in PBF-LB/M were recently published [13, 14]. To assess the

✉ Stefan Brenner
  stefan.brenner@unibw.de

[1] Institute for Design and Production Engineering, Werner-Heisenberg-Weg 39, 85577 Neubiberg, Germany

[2] Institute for Weapons Technology and Materials Science, Werner-Heisenberg-Weg 39, 85577 Neubiberg, Germany

[3] Department of Mechanical Engineering, University of the Bundeswehr Munich, Werner-Heisenberg-Weg 39, 85577 Neubiberg, Germany

morphology of powder layers, a method often used is to take high-resolution images during the process. The detection and classification of errors allow distinguishing between different types of recoater errors, such as wear and local damage [15] or recoater hopping and streaking [16].

To evaluate the effects of irregularities in the powder bed on the resulting defects in the printed parts, process errors are intentionally induced. Grasso [17] pre-damaged the recoater brush of an Electron Beam Melting machine to vary the severity of irregularities in the powder bed at specific locations. In several studies, damage-causing parts are intentionally printed to draw conclusions about resulting porosity formation in the printed parts [18], to compare the acquired images to parts with actual process defects, like failed support material [19], or to validate recoater crash simulations [7, 12, 20].

Previous studies focus on the formation of microstructural defects in parts printed with irregular powder bed conditions or mention qualitatively increased roughness [15]. Quantitative information on important quality aspects, such as tensile properties, dimensional accuracy, roughness, and hardness of parts printed under irregular powder bed conditions, is scarce.

The objective of this research is to intentionally cause recoater crashes to evaluate the quality of parts that are affected by powder bed irregularities during their fabrication.

2 Methods and samples

2.1 Design of damage-causing artifacts

To intentionally cause and assess powder bed irregularities, it is possible to pre-damage the recoating device [17] or to design parts in a way that they will lead to interference with the recoating device during the build job, damage it, and, therefore, cause powder bed irregularities [18, 19].

To follow the latter approach, a two-sided overhang was chosen as a design baseline for the damage-causing artifact, because such geometries are prone to show super-elevation, especially if the unsupported overhang angle is 45° or less [5, 12].

The proprietary PBF-LB/M simulation tool *Workbench Additive* within ANSYS Mechanical 2022R1 (ANSYS Inc., Canonsburg, USA) was used to produce numeric results for in-process distortions of unsupported overhangs. The main abstractions of the FE model include lumped *super layers*, which represented eight physical layers in this study, and the *heat application* by setting newly added *super layers* to the melting temperature, neglecting the scan strategy [21]. The default settings were maintained without calibrating the Strain Scaling Factor.

The design of the artifact had two goals:

1. To cause interference between the part edges and the recoater lip during the build job. Local damage at specific locations is necessary to place adjacent samples in recoating direction on the build plate, which will be affected by the resulting powder bed irregularities due to the damaged lip.
2. To ensure that only the recoater lip is affected and not the lip mount. This prevents collisions between part edges and rigid components of the recoater, which would likely result in wear or more severe machine damage. The design of the artifact is intended to allow the build job to continue with a damaged recoater lip. Therefore, the super-elevations of the overhang artifacts must remain within a certain target range for z-distortions.

A quarter-symmetry FE model was used with the critical part dimensions, as shown in Fig. 1. By varying the overhang angle α, the intensity of the super-elevation effect was studied.

Given the nominal layer thickness of 30 μm (Table 1), it might be conceivable to expect recoater crashes as soon as the maximum z-distortions z_{dist} exceed 30 μm. As it is known from the recent literature, the effective layer thickness (ELT) of powder above a part is significantly higher

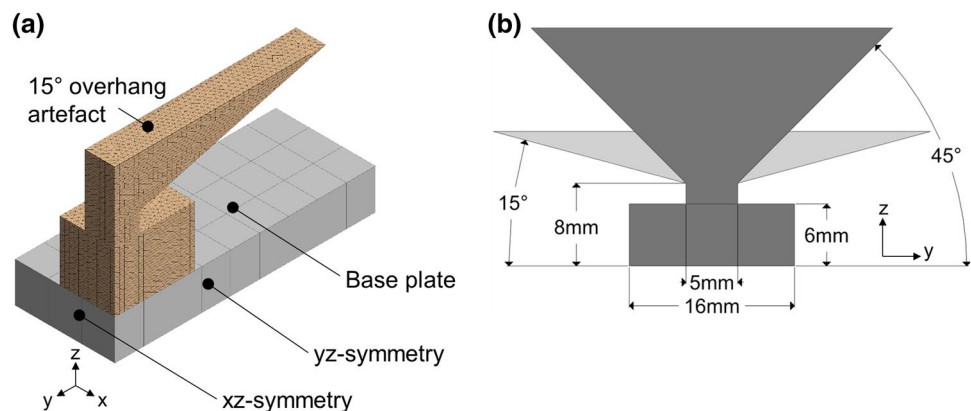Fig. 1 **a** Quarter-symmetry FE model and **b** critical overhang artifact dimensions

Table 1 Process parameters for sample fabrication

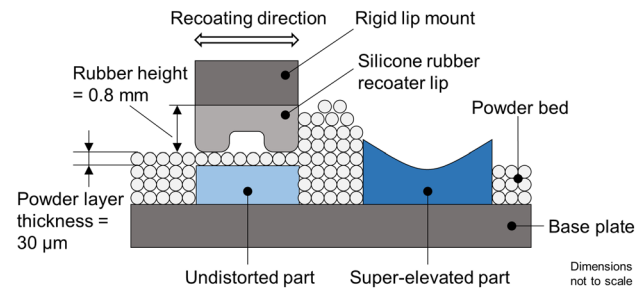| Process parameter	Value
Laser power [W]	350
Scan speed [mm/s]	1650
Hatch Distance [mm]	0.13
Layer thickness [µm]	30
Base plate temperature [°C]	150
Shielding gas	Argon 4.6

Fig. 2 Schematic of the recoater moving toward super-elevated part edges. The interference of the super-elevated part with the rubber recoater lip is referred to as recoater crash in this study. A collision between a part and the rigid lip mount is likely to result in wear or more severe machine damage

than the nominal value [22]. The ELT is reported to be 4 to 5.5 [23] or even more than 7.5 times [24] the nominal layer thickness. Reasons for this are shrinkage effects after solidification [24], formation of spatter and denudation [23]. Considering this behavior, the overhang artifacts have a target range for z-distortion of $0.2 \text{ mm} < z_{dist} < 0.8 \text{ mm}$, with the lower limit z_{min} given by $ELT \approx 0.2 \text{ mm}$ and the upper limit z_{max} given by the free rubber height of 0.8 mm (Fig. 2) to avoid collision with the rigid lip mount.

To select an appropriate overhang angle, the maximum z_{dist} on the top of each *super layer* is checked before adding the next *super layer* to determine if the target range is reached during the simulation.

Based on the above-mentioned characteristics, an appropriate artifact design must satisfy the distortion requirement $z_{min} < z_{dist} < z_{max}$ to be selected as a part of the build layouts which were planned as follows.

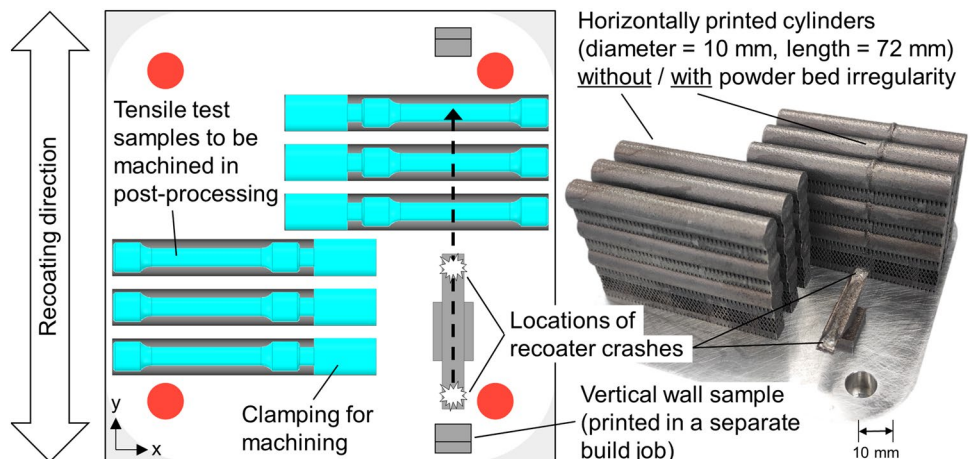## 2.2 Sample fabrication and build layout

The samples used for the experimental tests were printed from AlSi10Mg powder (20–63 µm) on an SLM 125HL machine (SLM Solutions AG, Germany) with a build size of $125 \times 125 \text{x} 125 \text{ mm}^3$. The main process parameters used for all build jobs in this study are listed in Table 1.

For each build job, a virgin silicone rubber recoater lip was used. The schematic in Fig. 2 shows super-elevated part edges that will likely interfere with the recoater lip.

Samples were placed adjacent to the damage-causing artifacts aligned with the recoating direction in build layouts similar to Bartlett et al. [18] and Foster et al. [19]. Stacks of three horizontal cylinders (diameter = 10 mm; length = 72 mm) were printed to evaluate tensile test properties (see Sect. 3.3). Figure 3 shows a representative build layout used in this study. The longitudinal orientation of the artifact was aligned with the recoating direction and the dotted line arrow indicates the expected transfer of powder bed irregularities from the artifact to the adjacent samples.

The cylinders were printed at three different build heights h_{build}, with the axes at z-positions of 18.4 mm, 31.4 mm, and 44.4 mm. This ensured that the samples were positioned above the artifact and thus printed with a damaged recoater lip. Block supports were used as a connection between the cylinders and to the base plate. In a post-processing step, the cylinders were machined to standardized tensile test samples

Fig. 3 Build layout with tensile test samples and a damage-causing overhang artifact. Vertical wall samples were positioned accordingly in recoating direction, but printed in a separate build job

(DIN50125-B5×25) with a diameter of 5 mm, as used in the VDI material data sheet for AlSi10Mg [25].

Vertical walls were printed in a separate build job to determine roughness, flatness tolerance, and hardness (see Sect. 3.4). Four overhang artifacts were located parallel with two vertical wall samples adjacent to each.

2.3 Recoater crash detection

The SLM 125HL machine is equipped with a Layer Control System (LCS) that takes 8-bit grayscale images after a new powder layer is spread. Therefore, for each build job, a stack of images was taken that corresponds to the number of layers. These images were analyzed to check for appearing powder bed irregularities, indicating local damages to the recoater lip. The image processing steps are shown in Fig. 4 for an exemplary stack of $n + k$ images. Because of an uneven illumination within the build chamber (Fig. 4a), the background of the images was removed utilizing the ImageJ software (National Institutes of Health, USA) to enable meaningful grayscale value measurements. To determine the beginning of a recoater crash, the grayscale value of each pixel was measured along several parallel profiles (dashed lines in Fig. 4b) in the x-direction in each image. The average value for each column of pixels was formed. From this, local changes in the grayscale values during a build job could be recognized and interpreted as appearing powder bed irregularities.
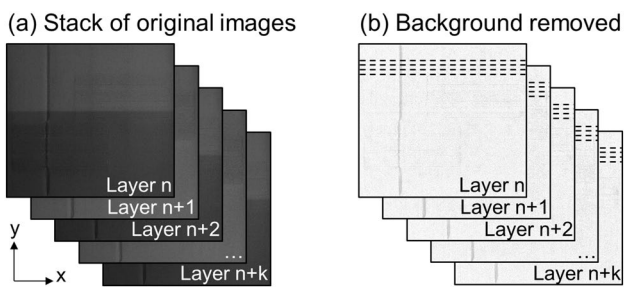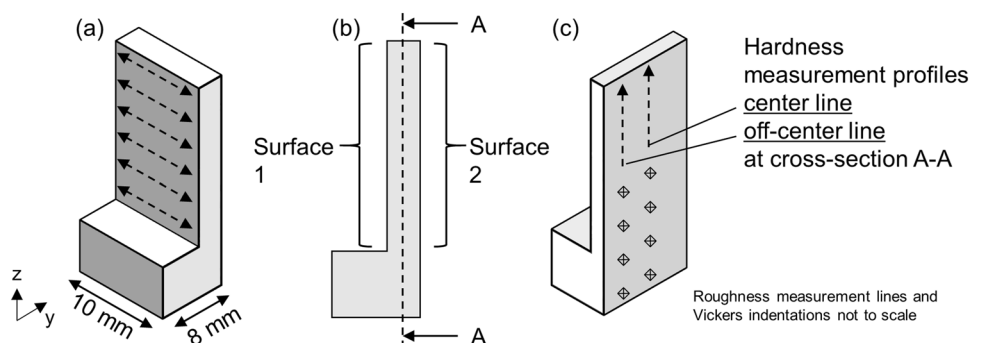
The control level for deciding whether a recoater crash occured was set to six times the standard deviation of a powder layer without irregularities at $h_{build} = 7.5$ mm, before the beginning of the overhang. Craeghs et al. [15] have used this control level successfully for a similar purpose.

The LCS can be used to evaluate if and when a recoater crash occurred during the build job. This information was used to validate the super-elevation of the overhang artifacts.

2.4 Static tensile tests

Static tensile tests according to DIN EN ISO 6892–1 were carried out on a Zwick/Roell testing machine (Z100, Zwick-Roell GmbH, Germany) to determine Young's modulus YM, yield strength YS, ultimate tensile strength UTS and elongation at break ε_{break}. A sample size of n = 3 was used for each combination of h_{build} and powder bed condition (irregular or reference). Fracture surfaces were examined using a digital microscope (VHX-2000, Keyence Co., Japan) with 50 × and 200 × magnification.

2.5 Surface measurements and hardness tests

The vertical wall samples were scanned with an optical profilometer (VR-5200, Keyence Co., Japan) using 40 × magnification and high-resolution mode. The device was also used for contour scans and profile measurements on damaged recoater lips.

The average roughness Ra was measured at parallel, horizontal lines with lengths of 7.5 mm on the vertical wall surfaces (Fig. 5a) with filter settings $\lambda_s = 25$ μm and $\lambda_c = 2.5$ mm. To compare regular and irregular powder bed conditions, areas were selected at build heights before and after the recoater crash.

Regarding the flatness tolerances, the height distance between the minimum and maximum of the topography at wall surfaces 1 and 2 (Fig. 5b) was measured in each case.

Next, the wall samples were embedded and ground. Vickers hardness HV0.5 was tested on cross-sections A-A (Fig. 5b) using a hardness tester (ecoHARD XM 1280 A, AHOTEC e.K., Germany). Measurement points with a
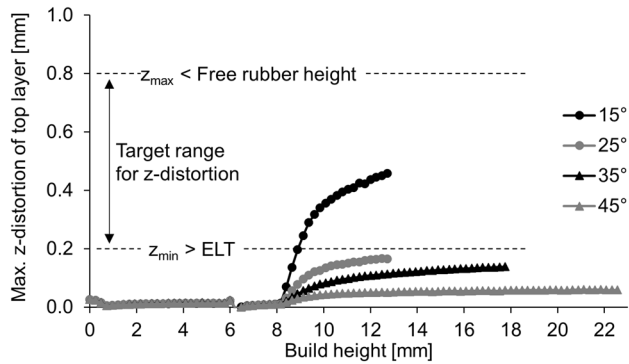

Fig. 4 LCS image processing steps with **a** stack of original images and **b** images after background removal

Fig. 5 Locations of **a** roughness and **c** Vickers hardness measurements. Flatness tolerances were measured on **b** Surface 1 and Surface 2

Fig. 6 Simulation results for in-process z-distortions of artifacts with overhang angles α of 15°, 25°, 35°, and 45°. Only the artifact with an overhang angle of 15° reaches the target range for z-distortion

spacing of 1 mm were placed in the z-direction long center and off-center lines (Fig. 5c).

3 Results and discussion

3.1 Simulation results

The simulation outputs of z_{dist} for every simulated *super layer* of the overhang artifacts with $15° < α < 45°$ are analyzed. Figure 6 shows the curves of z_{dist} of the current top *super layer* over h_{build}. The curves only differ from $h_{build} = 8$ mm, which is the beginning of the overhangs. The 15° overhang angle shows the steepest increase and crosses the z_{min} level at $h_{build} \approx 9$ mm. It reaches the highest z_{dist} of 0.46 mm but remains below z_{max}.

The results show a clear trend toward more pronounced super-elevation at smaller overhang angles $α$, which was also expected. Only the overhang artifact with $α = 15°$ reaches the target range for z_{dist}, indicating that this variant distorts sufficiently to damage the recoater lip, but does not distort enough to cause a collision with the rigid lip mount. Therefore, the 15° artifact is considered suitable to fulfill the purpose of causing recoater crashes without damaging the machine. Despite known limitations in the ability of simulation models to predict recoater crashes [12] and model abstractions (see Sect. 2.1), this design is selected as the damage-causing artifact for all build jobs in this study.

3.2 Simulation validation

The LCS images from a build job with four parallel overhang artifacts and two vertical wall samples adjacent to each artifact are analyzed to detect recoater crashes and validate the predicted in-process z-distortions from the simulation model. Super-elevated edges are slightly visible at $h_{build} \approx 9$ mm and clearly protrude from the powder bed at

$h_{build} = 10.5$ mm (Fig. 7a), but no irregularities are yet present (Fig. 7b). After the super-elevated edges have interfered with the recoater lip, the further powder layers are spread with a damaged lip, resulting in irregularities in the powder bed. The occurrence of irregularities is detected by LCS in the range of 10.8 mm $< h_{build} <$ 11.8 mm with some scatter between the four artifacts. At $h_{build} = 12.96$ mm (Fig. 7c), the irregularities are clearly visible and the grayscale measurements show downward spikes to values of about 230, which are significantly below the control level of 245.7 (Fig. 7d). The white arrow (Fig. 7c, middle) points to a torn-out piece of rubber from the damaged recoater lip.

After build job completion, the recoater lips exhibit two types of damage. First, there are notches in the lips (Fig. 8a,b) that are up to 1.5 mm deep and about 4 mm wide (Fig. 8e). Second, there are rubber snippets (Fig. 8c, d) that protrude downward from the lips by up to 1 mm (Fig. 8f).

The occurrence of super-elevations starting at $h_{build} \approx 9$ mm corresponds well with the simulated z_{dist} exceeding the z_{min} level at about this build height. The predicted further increase in z_{dist} can also be validated by the observed powder bed irregularities and the damage to the lips. Although some notches in the lips are deeper than the free rubber height (Fig. 2), the rigid lip mount remains unscathed. This suggests that the in-process z-distortions of the artifacts are less than z_{max}. The deep notches may be caused by abruptly torn-out rubber pieces and not by layer-by-layer wear. During the build job, pieces of rubber were found in the LCS images of several layers, as exemplified
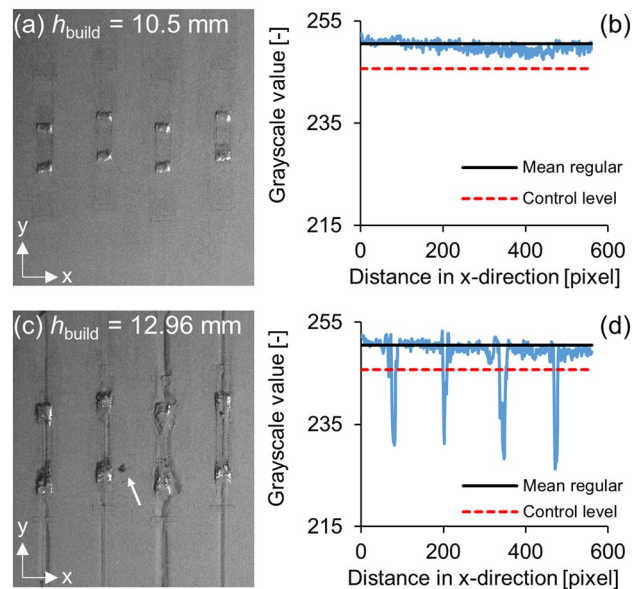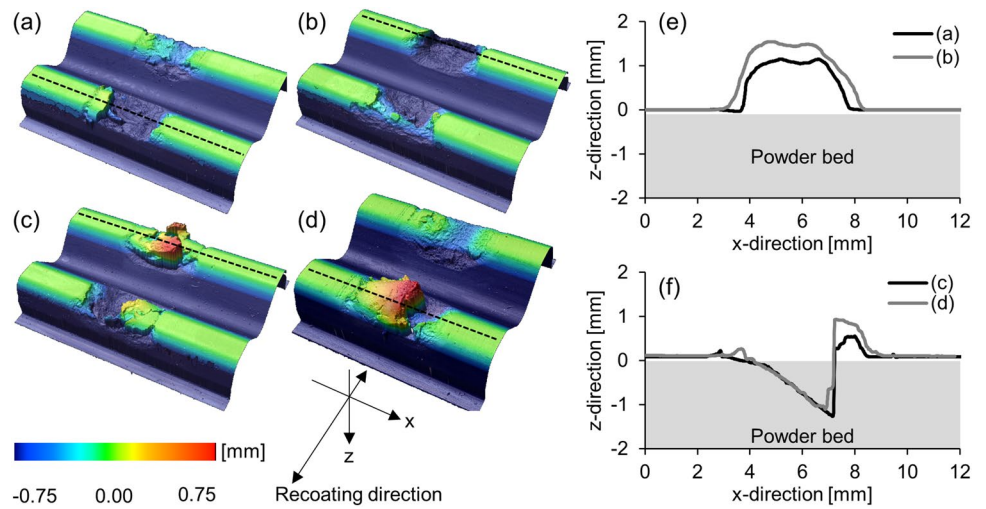

Fig. 7 Original LCS image of build heights 10.5 mm **a** and 12.96 mm **c** with corresponding grayscale value measurements **b** and **d**. Mean regular = 250.5, control level = mean–6xSD = 245.7. The white arrow in **c** points to a torn-out piece of rubber from the damaged recoater lip

Fig. 8 Scanned contour of recoater lips after crash with notch-type damage **a**, **b** and snippet-type damage **c**, **d**. Height profile of notch-type damage **e** and snippet-type damage **f**. Dashed lines in **a-d** show the profile lines of **e** and **f**

in Fig. 7c. The protruding snippets may have been flexible enough to bend but not be torn out when they passed the super-elevated edges during the recoater movement.

Based on these findings, the simulative prediction of interference between the super-elevated edges and the recoater lips shows good agreement with the experiments. The overhang artifacts meets the requirements to cause powder bed irregularities, but no damage to the machine.

3.3 Tensile properties

The samples show different behavior depending on the type of damage to the recoater lip. One representative stress–strain curve is plotted in Fig. 9a each for samples printed with a regular powder bed as reference (dotted line), with irregularities from snippet-type damages (black line) and with notch-type damages (gray line). The samples with snippet-type damages perfectly follow the reference curves, but break at low ε_{break} of 1% to 3%, depending on their h_{build}. Large areas of unmelted powder particles are found on the fracture surfaces (Fig. 9b). The samples

with notch-type damages yield earlier, however, show plastic deformation up to an ε_{break} of 8.8% at $h_{build} = 18.4$ mm. Only a few unmelted particles are observed on the fracture surfaces (Fig. 9c). From the build job with notch-type damages, only samples from $h_{build} = 18.4$ mm are available.

For all samples, a *YM* of approximately 70 GPa is measured, which is not influenced by the powder bed condition or h_{build}.

YS decreases from 282 to 245 MPa as h_{build} increases from 18.4 mm to 44.4 mm for reference samples and snippet-type damages. For notch-type damages, a *YS* of 243 MPa is measured at $h_{build} = 18.4$ mm, which is the same as the other samples decrease to at $h_{build} = 44.4$ mm.

UTS decreases from 447 to 424 MPa as h_{build} increases from 18.4 mm to 44.4 mm for reference samples. For snippet-type damages, a lower general *UTS* level of 335 MPa to 361 MPa is observed with no clear relationship to h_{build}. For notch-type damages, a *UTS* of 422 MPa is measured at $h_{build} = 18.4$ mm, which again corresponds to the level of the reference samples at $h_{build} = 44.4$ mm.

Fig. 9 **a** Engineering stress–strain curves for samples with regular and irregular powder bed conditions and fracture surfaces for **b** snippet-type damage and **c** notch-type damage. For better readability, only one representative stress–strain curve is shown each
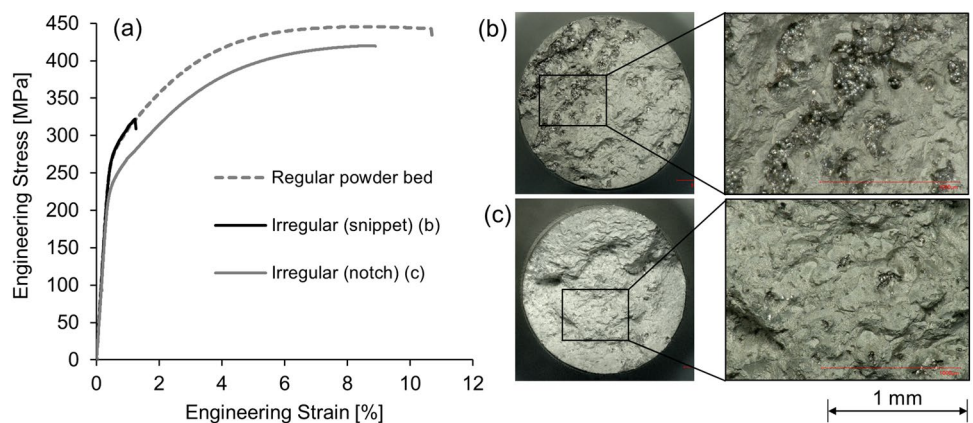
Table 2 provides the results overview given as mean and standard deviation.

The unmelted particles, which are found on the fracture surfaces, suggest that the powder bed irregularities cause lack-of-fusion (LoF) defects. LoF porosity was reported at overhangs [7] and as a result of incomplete melting of uneven powder layers [26]. Bartlett et al. [18] described that both powder pile-up and powder recess cause LoF defects, the former because of decreased beam penetration and therefore insufficient heating, the latter because of poor powder packing density and altered physical size of the layer that changes the effective conductivity of the powder bed. Looking at the shapes of the damaged lips in Fig. 8, it is conceivable, on the one hand, that powder piles up above the powder bed level below the notch, forming visible streaks. On the other hand, downward protruding snippets conceivably dig into the powder bed and cause powder recess, which forms visible grooves. From the LCS images, it is not possible to determine the shape of the irregularities.

Snippet-type damages are found to have no effect on YM and YS, but to decrease UTS by 15% to 25% depending on h_{build} and a sharp drop is observed for ε_{break}. It is known that h_{build} affects the mechanical properties in PBF-LB/M [27, 28]. In the reference build jobs of this study, YS and UTS decrease as h_{build} increases, which is in contrast to the findings of Weiss et al. [28]. In the case of the build job with the notch-type damage, the printing process was stopped after the completion of the horizontal cylinders at $h_{build} = 18.4$ mm. These samples, therefore, experienced a different thermal history than the samples from other build jobs, where additional cylinders were printed above them.

The findings reported in this study suggest that certain tensile properties are similarly dependent on the powder bed condition and the thermal history within the investigated build height range. Further research is required to gain a better understanding of these effects.

To put the tensile properties into context, mean values below or above the limits of the VDI-Standard [25] are marked in Table 2. Only samples from snippet-type damages fall below the lower limits of UTS and ε_{break}. All measured elastic properties (YM and YS) in this study are within the limits of the VDI-Standard, while the reference samples and the notch-type damages even exceed the upper end of the range for ε_{break}. Therefore, the presence of LoF defects from powder bed irregularities has no noticeable effect on the elastic properties.

3.4 Flatness tolerance, roughness, and Vickers hardness

The defects in the sample surfaces are clearly visible (Fig. 10a) and the samples show distinct build heights $h_{crash,Surf}$ at which the recoater lips are damaged (Fig. 10b). Large LoF defects are found in the cross-sections (Fig. 10c, d) at $h_{crash,Cross-sect}$. The effects are independent of the damage type of the recoater lip.

The flatness tolerances almost double from 0.24 mm to 0.44 mm and the roughness Ra increases by 40% from 6.2 μm to 8.7 μm due to powder bed irregularities. Vickers hardness remains constant at HV0.5 = 120, both along the center line and along the off-center line. The measurements are summarized in Table 3.

Table 2 Overview of tensile test results

Property	Powder bed condition	Build height [mm]		
		18.4	31.4	44.4
YM [GPa]	Regular	72.3*±4.2*	70.2±0.6	67.8±2.0
	Irregular (snippet)	69.0±0.4	69.6±1.7	69.8±1.5
	Irregular (notch)	69.3±4.6	–	–
YS [MPa]	Regular	282.4±2.0	274.0±1.4	244.6±1.9
	Irregular (snippet)	284.6±1.2	275.0±2.2	245.8±1.0
	Irregular (notch)	243.3±0.6	–	–
UTS [MPa]	Regular	447.1±1.8	441.0±1.5	424.3±2.1
	Irregular (snippet)	335.5[a)]±20.2	361.6[a)]±12.1	361.4[a)]±3.0
	Irregular (notch)	422.4±1.9	–	–
ε_{break} [%]	Regular	10.0[b)]±0.5	10.3[b)]±0.3	11.1[b)]±0.4
	Irregular (snippet)	1.0[a)]±0.4	1.8[a)]±0.3	2.7[a)]±0.1
	Irregular (notch)	8.8[b)]±0.8	–	–

All results are given as mean ± standard deviation

For Irregular (notch) only Build height = 18.4 mm was tested

[a)]Mean below limits of material data sheet for AlSi10Mg in VDI standard [25]

[b)]Mean above limits of material data sheet for AlSi10Mg in VDI standard [25]

*One supposed upwards outlier (YM = 77 GPa) due to a clamping error included

Fig. 10 **a** As-built vertical wall sample with surface topography **b**. Cross-section of embedded and ground sample **c** with detail of defect **d**
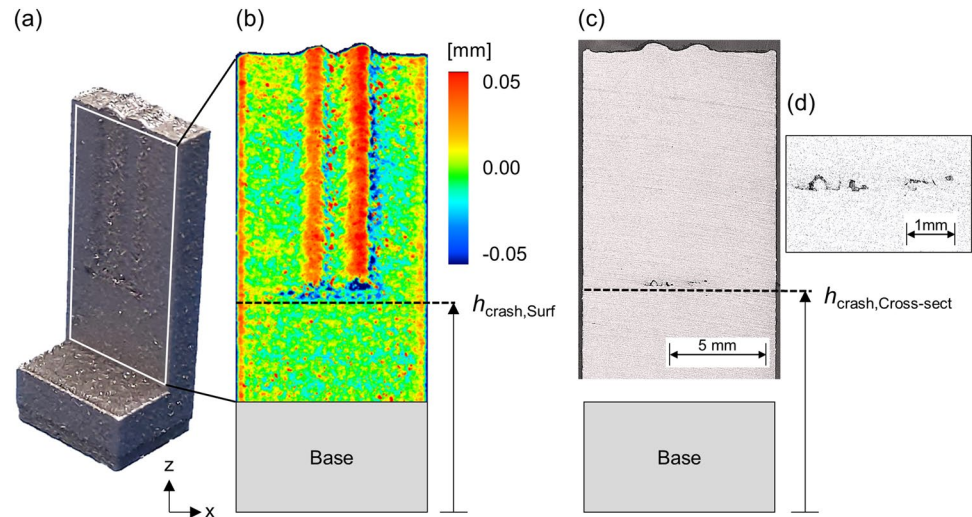

4 Conclusion

To evaluate the resulting quality of parts when recoater crashes occur in the PBF-LB/M process, FE simulations are used to design damage-causing artifacts that intentionally cause recoater crashes. The experimental results show the influence of powder bed irregularities on important quality aspects of samples adjacent to the damage-causing artifacts.

The FE simulations of in-process distortions are used for designing efficient artifacts that intentionally damage the recoater lips but avoid machine breakdown. The design that shows suitable simulation results is printed and validated. The predicted target range for the z-distortion is reached. Therefore, FE process simulations are useful to predict the interference between parts and the recoater.

The experimental results show only little effect of powder bed irregularities on elastic tensile properties. Young's modulus and yield strength of the samples remain within the limits of the corresponding material data sheet in the VDI-Standard for AlSi10Mg. In damage-affected samples, lack-of-fusion defects and decreased elongation at break are found. In certain samples, fracture occurs with an elongation at break of only 1% compared to 10% in undamaged reference samples. In other samples, an elongation at break of 8.8% is measured, which is higher than the value specified in the VDI-Standard. It should be emphasized that the sample size in this experiment is small and the samples are machined before testing. In the as-built condition, the observed defects in the sample surfaces will act as notches and possibly cause earlier failure. No decrease in hardness due to recoater crashes is observed. Visible defects on the surfaces deteriorate dimensional accuracy and roughness, but could possibly be removed in post-processing steps to improve the usability of the parts.

Table 3 Overview of the results for flatness tolerance, roughness, and Vickers hardness

Powder bed condition	Property		
	Flatness tolerance [mm]	Roughness R_a [µm]	Vickers hardness [$HV_{0.5}$]
Regular	0.24 ± 0.03	6.2 ± 1.3	120.2 ± 1.8
Irregular	0.44 ± 0.11	8.7 ± 2.8	120.0 ± 2.6

All results are given as mean $\pm$ standard deviation

Several studies report similar phenomena, such as stripes and swelling defects [15, 17, 29]. Contour defects deteriorate the dimensional accuracy and roughness of the parts, but can be removed during post-processing if accessibility is given. For filigree structures, there is a risk of failure if the contour defect is large in relation to the feature thickness, e.g., in lattice structures.

Grasso [17] found areas of LoF porosity that vary in size depending on the severity of the powder bed irregularity below the swelling defects in Electron Beam Melting. Bartlett et al. [18] showed a relationship between the severity of powder bed errors and the formation of microstructural defects in PBF-LB/M as well. The exemplary LoF defect in Fig. 10 is located just above the crash height and is limited in the z-extension. In the further printing process with damaged recoater lip, no more noticeable defects are found in the wall samples. This is contrary to the tensile samples, where the unmelted powder is found subsequent to the crash height.

Overall, even when recoater crashes occur, parts from these build jobs are not necessarily reject and might be usable, especially for static loading below yield strength and considering a reduced margin of safety taking into account microstructural defects and notch effects of as-built surface conditions.

Nevertheless, powder bed irregularities are still an area of concern in PBF-LB/M, especially for dynamic loads. The detection, classification, and simulative prediction of such process errors constitute growing research fields. Process simulation along with process monitoring is useful tool to optimize part designs and build layouts.

This study contributes quantitative results on important part quality aspects to evaluate the effects of powder bed irregularities. With this knowledge available, PBF-LB/M users can make appropriate decisions about the affected parts, to reduce reject, avoid machine downtime, and therefore increase productivity.

Declarations

References

1. DebRoy T, Wei HL, Zuback JS, Mukherjee T, Elmer JW, Milewski JO, Beese AM, Wilson-Heid A, De A, Zhang W (2018) Additive manufacturing of metallic components-Process, structure and properties. Prog Mater Sci 92:112–224. https://doi.org/10.1016/j.pmatsci.2017.10.001

2. Zaeh MF, Branner G (2010) Investigations on residual stresses and deformations in selective laser melting. Prod Eng Res Devel 4:35–45. https://doi.org/10.1007/s11740-009-0192-y

3. Levkulich NC, Semiatin SL, Gockel JE, Middendorf JR, DeWald AT, Klingbeil NW (2019) The effect of process parameters on residual stress evolution and distortion in the laser powder bed fusion of Ti-6Al-4V. Addit Manuf 28:475–484

4. Scime L, Beuth J (2018) A multi-scale convolutional neural network for autonomous anomaly detection and classification in a laser powder bed fusion additive manufacturing process. Addit Manuf 24:273–286. https://doi.org/10.1016/j.addma.2018.09.034

5. Kleszczynski S, zur Jacobsmühlen J, Sehrt JT, Witt G (2012) Error detection in laser beam melting systems by high resolution imaging. in: 23rd annual international solid freeform fabrication symposium: an additive manufacturing conference. University of Texas at Austin, 975–987

6. zur Jacobsmühlen J, Kleszczynski S, Schneider D, Witt G (2013) High resolution imaging for inspection of laser beam melting systems. In: 2013 IEEE international instrumentation and measurement technology conference (I2MTC), 707–712

7. Yavari R, Smoqi Z, Riensche A, Bevans B, Kobir H, Mendoza H, Song H, Cole K, Rao P (2021) Part-scale thermal simulation of laser powder bed fusion using graph theory: effect of thermal history on porosity, microstructure evolution, and recoater crash. Mater Des 204:109685. https://doi.org/10.1016/j.matdes.2021.109685

8. Morante F, Palladino M, Lanzetta M (2020) Towards an integrated sensor system for additive manufacturing. In: Da Silva Bartolo PJ, Da Silva FM, Jaradat S et al (eds) Industry 4.0–shaping the future of the digital world. CRC Press, Boca Raton, pp 173–178

9. Westphal E, Seitz H (2021) A machine learning method for defect detection and visualization in selective laser sintering based on convolutional neural networks. Addit Manuf 41:101965. https://doi.org/10.1016/j.addma.2021.101965

10. Xiao L, Lu M, Huang H (2020) Detection of powder bed defects in selective laser sintering using convolutional neural network. Int J Adv Manuf Technol 107:2485–2496. https://doi.org/10.1007/s00170-020-05205-0

11. Afazov S, Roberts A, Wright L, Jadhav P, Holloway A, Basoalto H, Milne K, Brierley N (2022) Metal powder bed fusion process chains: an overview of modelling techniques. Prog Addit Manuf 7:289–314. https://doi.org/10.1007/s40964-021-00230-1

12. Peter N, Pitts Z, Thompson S, Saharan A (2020) Benchmarking build simulation software for laser powder bed fusion of metals. Addit Manuf 36:101531. https://doi.org/10.1016/j.addma.2020.101531

13. Wu B, Ji X, Zhou J, Yang H, Peng D, Wang Z, Wu Y, Yin Y (2021) In situ monitoring methods for selective laser melting additive manufacturing process based on images—A review. China Foundry 18:265–285. https://doi.org/10.1007/s41230-021-1111-x

14. McCann R, Obeidi MA, Hughes C, McCarthy É et al (2021) In-situ sensing, process monitoring and machine control in Laser Powder Bed Fusion: a review. Addit Manuf 45:102058. https://doi.org/10.1016/j.addma.2021.102058

15. Craeghs T, Clijsters S, Yasa E, Kruth J-P (2011) Online quality control of selective laser melting. In: 22nd annual international solid freeform fabrication symposium: an additive manufacturing conference. University of Texas at Austin, 212–226

16. Scime L, Siddel D, Baird S, Paquit V (2020) Layer-wise anomaly detection and classification for powder bed additive manufacturing processes: a machine-agnostic algorithm for real-time pixel-wise semantic segmentation. Addit Manuf 36:101453. https://doi.org/10.1016/j.addma.2020.101453

17. Grasso M (2021) In Situ monitoring of powder bed fusion homogeneity in electron beam melting. Materials. https://doi.org/10.3390/ma14227015

18. Bartlett JL, Jarama A, Jones J, Li X (2020) Prediction of microstructural defects in additive manufacturing from powder bed quality using digital image correlation. Mater Sci Eng A 794:140002. https://doi.org/10.1016/j.msea.2020.140002

19. Foster BK, Reutzel EW, Nassar AR, Hall BT, Brown SW, Dickman CJ (2015) Optical, layerwise monitoring of powder bed fusion. In: 26th annual international solid freeform fabrication symposium: an additive manufacturing conference. University of Texas at Austin, 295–307

20. Kobir MH, Yavari R, Riensche AR, Bevans BD, Castro L, Cole KD, Rao P (2022) Prediction of recoater crash in laser powder bed fusion additive manufacturing using graph theory thermo-mechanical modeling. Prog Addit Manuf. https://doi.org/10.1007/s40964-022-00331-5

21. ANSYS Inc. (2022) Ansys workbench additive manufacturing analysis guide: release 2022 R1, Canonsburg, PA

22. Jansen D, Hanemann T, Radek M, Rota A, Schröpfer J, Heilmaier M (2021) Development of actual powder layer height depending on nominal layer thicknesses and selection of laser parameters. J Mater Process Technol 298:117305. https://doi.org/10.1016/j.jmatprotec.2021.117305

23. Wischeropp TM, Emmelmann C, Brandt M, Pateras A (2019) Measurement of actual powder layer height and packing density in a single layer in selective laser melting. Addit Manuf 28:176–183. https://doi.org/10.1016/j.addma.2019.04.019

24. Mahmoodkhani Y, Ali U, Imani Shahabad S, Rani Kasinathan A, Esmaeilizadeh R, Keshavarzkermani A, Marzbanrad E, Toyserkani E (2019) On the measurement of effective powder layer thickness in laser powder-bed fusion additive manufacturing of metals. Prog Addit Manuf 4:109–116. https://doi.org/10.1007/s40964-018-0064-0

25. VDI-Standard 3405 Part 2.1 (2020) Additive manufacturing processes: powder bed fusion of metal with laser beam (PBF-LB/M). Material data sheet aluminium alloy AlSi10Mg

26. Yadav P, Rigo O, Arvieu C, Le Guen E, Lacoste E (2020) In situ monitoring systems of the SLM process: on the need to develop machine learning models for data processing. Crystals 10:524. https://doi.org/10.3390/cryst10060524

27. Mohr G, Altenburg SJ, Hilgenberg K (2020) Effects of inter layer time and build height on resulting properties of 316L stainless steel processed by laser powder bed fusion. Addit Manuf 32:101080. https://doi.org/10.1016/j.addma.2020.101080

28. Weiss C, Haefner CL, Munk J (2022) On the influence of AlSi10Mg powder recycling behavior in the LPBF process and consequences for mechanical properties. JOM 74:1188–1199. https://doi.org/10.1007/s11837-021-05080-4

29. Diegel O, Nordin A, Motte D (2019) Design for metal AM. A practical guide to design for additive manufacturing: springer series in advanced manufacturing. Springer, Singapore, pp 121–155